LASER & PHOTONICS REVIEWS
www.lpr-journal.org

Artificial Gauge Field Enabled Low-Crosstalk, Broadband, Half-Wavelength Pitched Waveguide Arrays

Peiji Zhou, Ting Li, Yucheng Lin, Lipeng Xia, Li Shen, Xiaochuan Xu, Tao Li, and Yi Zou**

Dense waveguide arrays with half-wavelength pitch, low-crosstalk, broadband, and flexible routing capability are essential for integrated photonics. However, achieving such performance is challenging due to the relatively weaker confinement of dielectric waveguides and the increased interactions among densely packed waveguides. Here, leveraging the artificial gauge field mechanism, half-wavelength-pitched dense waveguide arrays, consisting of 64 waveguides, in silicon with −30 dB crosstalk suppression from 1480 to 1550 nm are demonstrated. The waveguide array features negligible insertion loss for 90° bending. This approach enables flexibly routing a large-scale dense waveguide array that significantly reduces on-chip estate, leading to a high-density photonic integrated circuit, and may open up opportunities for important device performance improvement, such as half-wavelength-pitch optical phased array and ultra-dense space-division multiplexing.

1. Introduction

Waveguide arrays are among the fundamental building blocks for integrated photonics. A dense waveguide array could enable high-density integration of waveguide elements, significantly reducing on-chip estate and cost, for example, optical delay lines,[1,2] which usually occupy the largest on-chip area and hamper further improvements of integration density. On the other hand, a dense waveguide array could improve the devices' performance, such as a wider field of view for an on-chip optical phased array (OPA).[3–6] OPAs are based on optical diffraction in the free space, and they can transform the optical spatial distribution into the emission angles. The range of the steerable angles of an OPA is inversely related to the pitch of periodically arrayed emitters. In theory, achieving a 180° beam-steering range requires a half-wavelength pitched waveguide array. In addition, a dense waveguide array is also crucial in space-division multiplexing,[7] optical interconnection,[8,9] and wavelength-division multiplexers.[10,11]

Due to the increasing quantum tunneling effect of the photons from one waveguide to its neighbors, direct reducing the waveguide separations will result in a crosstalk boost that hinders the independent control of signal in a waveguide. While plasmonic waveguides can significantly suppress crosstalk,[12] the metallic loss issue limits its application.[13,14] Therefore, people mainly focus on all-dielectric waveguide solutions. Compared with metallic waveguides, light confinement in dielectric waveguides is relatively weaker, making the dense-packed dielectric waveguide array even more challenging. To tackle this issue, several approaches have been proposed,[15–19] such as inverse design,[15] anisotropic metamaterial cladding,[16] asymmetrical nano-waveguide,[17] waveguide super-lattice,[18] and bent waveguides,[19] showing significant crosstalk suppression for waveguide arrays with subwavelength pitch. However, these approaches either require small feature sizes (<100 nm), which are not compatible with the current photonics foundries that typically have a minimum feature of 150 nm, or lack scalable bending solutions, which are essential for on-chip flexible routing. Especially, the bending of a dense waveguide is challenging due to additional crosstalk from light leakage at bends. As a result, there is a high demand for devices with new design principles involved.

Gauge fields are a fundamental concept in physics that governs the interactions between charged particles. For neutral particles,

P. Zhou, T. Li, Y. Lin, L. Xia, Y. Zou
School of Information Science and Technology
ShanghaiTech University
Shanghai 201210, China
E-mail: zouyi@shanghaitech.edu.cn
T. Li
Shanghai Institute of Microsystem and Information Technology
Chinese Academy of Sciences
Shanghai 200050, China
T. Li
University of Chinese Academy of Sciences
Beijing 100049, China
L. Shen
Wuhan National Laboratory for Optoelectronics and School of Optical and Electronic Information
Huazhong University of Science and Technology
Wuhan, Hubei 430074, China
E-mail: lishen@hust.edu.cn
X. Xu
State Key Laboratory on Tunable Laser Technology
Harbin Institute of Technology
Xili University Town, Harbin Institute of Technology campus, Shenzhen, Guangdong 518055, China
T. Li
National Laboratory of Solid State Microstructures, Key Laboratory of Intelligent Optical Sensing and Integration, Jiangsu Key Laboratory of Artificial Functional Materials, College of Engineering and Applied Sciences
Nanjing University
Nanjing 210093, China

The ORCID identification number(s) for the author(s) of this article can be found under https://doi.org/10.1002/lpor.202200944

DOI: 10.1002/lpor.202200944

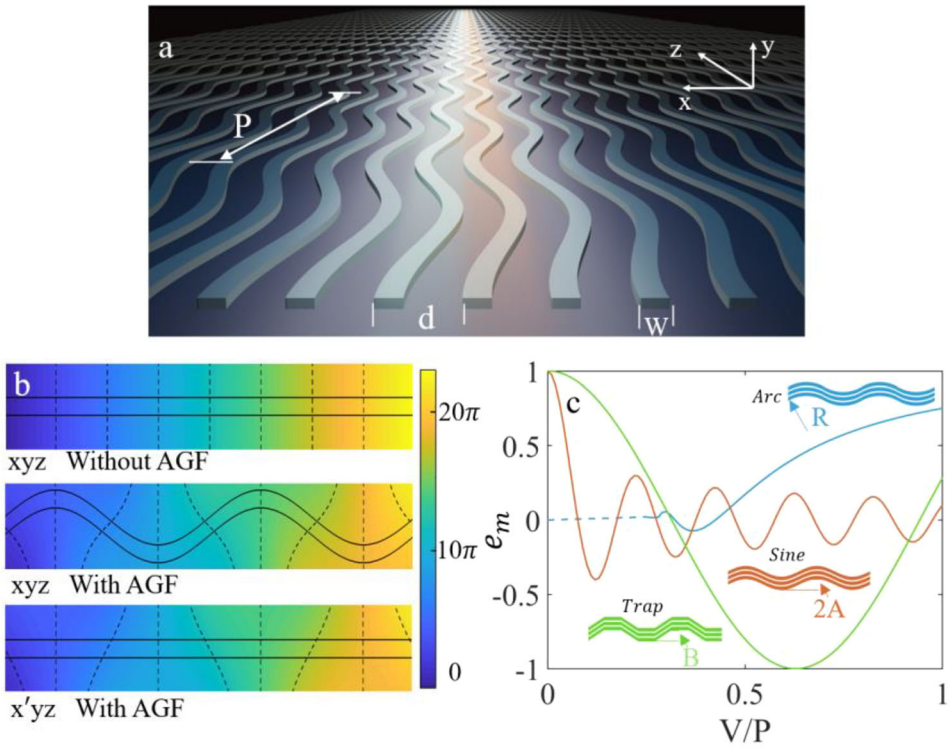

Figure 1. a) Schematic of the AGF-based waveguide array. b) Phase distribution along waveguides. The dashed lines indicate the equiphase surfaces. The upper, middle, and lower panels correspond to the waveguide without an AGF in *xyz* space, with an AGF in *xyz* space, and with an AGF in *x′yz* space, respectively. c) The coupling coefficient variation factor e_m for different AGF parameters $\frac{V}{P}$ when $k_0 n_s md = 5$, where V represents the structure parameters of different waveguide arrays, that is, V equals A, B, and R for the waveguide array with arc (blue), sinusoidal (orange), and trapezoid (green) shapes, respectively. Note that, for a waveguide array with arc-shape, there is no value for $R/P < 0.25$, which is the minimum achievable value. Insets show the shapes of the three waveguide arrays.

such as photons, one can generate artificial gauge fields (AGF) by properly engineering a physical system through geometric design or external modulations. The use of an AGF provides a new approach to photon manipulation and leads to a wide range of applications, such as dynamic localizations,[20–24] Floquet topological insulators,[25–27] and non-reciprocal devices using temporally modulated silicon photonics.[28] Recently, AGF-assisted light guiding has been proposed and demonstrated,[29–32] opening a new door for exploring on-chip light guiding, coupling, and routing.

In this paper, we develop an AGF-based coupling mechanism and experimentally demonstrate a strong coupling suppression would achieve in a dense waveguide array, even with a half-wavelength pitch. The AGF-induced exceptional coupling is observed with minimum crosstalk of ←35 dB at the wavelength of 1520 nm in the 750 nm pitched waveguide array, of which the pitch is even smaller than half of the wavelength. This ultra-dense waveguide array features negligible insertion loss and a working bandwidth of ≈40 nm with −20 dB crosstalk. Furthermore, we also demonstrate a bent 64-channel ultra-dense (750 nm pitch) waveguide array, possessing −30 dB crosstalk suppression from 1480 to 1550 nm and a more than 100 nm bandwidth with −25 dB crosstalk. Our approach enables significant on-chip estate reduction, leading to a high-density photonic integrated circuit, and may open up opportunities for important device performance improvement, for example, half-wavelength-pitched OPA and ultra-dense space-division multiplexing.

2. The Modulated Straight Waveguide Array

In a quantum system, wavefunctions can easily propagate through weak potential barriers. This is the so-called quantum tunneling effect. Analogous to the quantum system, there is significant crosstalk in a dense waveguide array due to increased interactions between the evanescent wave and nearby waveguides. However, introducing an AGF to a quantum system would generate an additional phase that may suppress the quantum tunneling effect.[33] We thus expect to reduce the crosstalk of a dense waveguide array by introducing an AGF. Since an AGF can be induced through spatial variations or external modulations, we would like to design specific structures to arouse an AGF that may change the interaction between two quantum states and, consequently, the energy band structure.

Figure 1a displays the proposed AGF waveguide array. Each waveguide has a periodically modulated trajectory $x_0(z)$. Unlike a straight waveguide, which has an equiphase surface perpendicular to the propagation direction z (the upper panel of Figure 1b), the AGF induces an additional x-dependent phase Λ that changes the spatial distribution of the equiphase, as shown in the middle

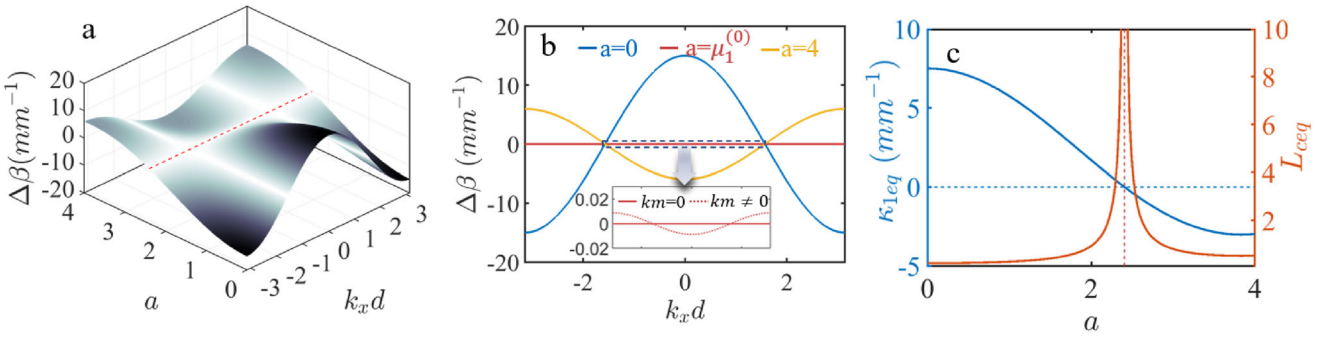

Figure 2. a) 3D view of the first Brillouin zone band diagram of the sinusoidal waveguide array as a function of $a = k_0 n_s \Omega A d$ and $k_x d$. The red dashed line corresponds to $a = \mu_1^{(0)}$, which is a horizontal line. b) The band structure for three fixed a. The blue, red, and yellow curves correspond to $a = 0$, $a = \mu_1^{(0)}$, and $a = 4$, respectively. The inset shows the enlarged view of the $a = \mu_1^{(0)}$. The solid and dotted lines represent $\kappa_m = 0$ $(m > 1)$ and $\kappa_m \neq 0$ $(m > 1)$, respectively. c) The equivalent coupling coefficient (left)/length (right) of the nearest neighbors κ_{1eq} (blue solid line)/L_{ceq} (the red solid line) as a function of a. The blue and red dashed lines represent $\kappa_{1eq} = 0$ and $a = \mu_1^{(0)}$, respectively.

panel of Figure 1b. To analyze it, we do a coordinate transformation, $x' = x - x_0(z)$, to convert the curved waveguide (the middle panel of Figure 1b) to the straight waveguide in the $x'yz$ space (the lower panel of Figure 1b), resulting in a tilted equiphase surface along the propagation direction z. Such a tilted equiphase surface may significantly affect the energy band structure of a waveguide array. When $x_0(z) = -x_0(z + \frac{P}{2})$, where P is the period of the AGF along the propagation direction z, the equivalent propagation constant β_{peq} in the waveguide array is (see Note S1, Supporting Information, for details):

$$\beta_{peq} = \beta_0 + \kappa_0 + 2\sum_{m>0} \cos\left(k_x m d\right) \kappa_{meq} \tag{1}$$

Here, β_0 is the propagation constant of an isolated straight waveguide. k_x is the momentum of the corresponding Bloch state. d is the pitch of the waveguide array. $\kappa_{meq} = e_m \kappa_m$ is the equivalent coupling coefficient of the curved waveguide array. κ_m is the coupling coefficient between the states of the m_1th and the m_2th waveguide of this system ($|m_1 - m_2| = |m|$). We then define $e_m = \overline{\cos(k_0 n_s \dot{x}_0(z) m d)}$ $(m > 0)$ as the AGF-induced coupling coefficient variation factor of κ_m, where k_0 is the momentum of a photon in a vacuum, $\dot{x}_0(z)$ is the derivative of $x_0(z)$ with respect to z, and n_s is the refractive index of the substrate. Therefore, the curved waveguide array has a similar energy spectrum to the straight waveguide array[34] by replacing κ_m with κ_{meq}.

From the definition of e_m, we obtain that $e_m \leq 1$, that is, $|\kappa_{meq}| \leq \kappa_m$, indicating suppression of quantum tunneling by introducing an AGF. In other words, the straight waveguide array without an AGF usually has the highest crosstalk. Applying an AGF to a waveguide array will generate an additional phase that tilts the equiphase surface and modifies the coupling coefficients from real numbers to z-dependent complex numbers with the same magnitude. Due to angle cancellation, the average value of multiple complex numbers tends to be lower than that of real numbers, analogous to the coherent cancellation of complex amplitudes of light fields. Note that this is a general conclusion regardless of the forms of the AGF as far as it is under the paraxial approximation premise. A special case happens when $e_1 = 0$, and consequently, we have $\kappa_{1eq} = 0$, indicating a complete suppression of the coupling from the nearest neighbors, the major source of crosstalk in a waveguide array. When $\kappa_{1eq} = 0$ and ignoring all the $m > 1$ terms, the band structure becomes $\beta_{peq} = \beta_0 + \kappa_0$, corresponding to a horizontal line in the energy spectrum shown in **Figure 2**b. In this situation, all Bloch solutions degenerate and evolve spatially dispersionless in the system with identical phase velocity.

To get an insight, we calculate band diagrams for three waveguide arrays with different types of AGF (insets of Figure 1c), namely the sinusoidal, trapezoidal splicing, and arc splicing trajectories (see Note S1, Supporting Information, for details). The coupling coefficient variation factor e_m is plotted in Figure 1c as a function of $\frac{V}{P}$ when $k_0 n_s m d = 5$, where V represents the structure parameters of different waveguide arrays, that is, V equals A, B, and R for the waveguide array with arc (blue), sinusoidal (orange), and trapezoid (green) shapes, respectively. Here, A is the amplitude of the sinusoidal curve (orange), $\frac{B}{P}$ represents the slope of the trapezoid shape (green), and R is the radius of the arc (blue). For all cases, there exist points that $e_m = 0$, corresponding to the AGF-induced coherent destruction of tunneling (CDT), independent of the form of the AGF.

The sinusoidal curve is selected for our later design for its smooth curvature and continuous change of radius of curvature properties. In this case, the AGF-induced coupling coefficient variation factor becomes $e_m = J_0(ma)$, where $J_0(x)$ is the 0th Bessel function, $a = k_0 n_s \Omega A d$, and $\Omega = \frac{2\pi}{P}$ is the spatial angular frequency of the sinusoidal curve. The corresponding equivalent coupling coefficient of the nearest neighbors in the sinusoidal waveguide array is $\kappa_{1eq} = \kappa_1 J_0(a)$ (see Note S1, Supporting Information, for details). Figure 2a shows the first Brillouin zone band diagram of the sinusoidal waveguide array. Figure 2b is the band structure for $a = 0$, $a = \mu_1^{(0)}$, and $a = 4$. $\mu_s^{(t)}$ stands for the sth zero of the tth Bessel function, so $\mu_1^{(0)}$ is the first zero of the 0th Bessel function. For a fixed a, the dispersion relationship is a cosine curve. Note that since the curves of $\kappa_m = 0$ $(m > 1)$ (solid) and $\kappa_m \neq 0$ $(m > 1)$ (dotted) almost coincide, which is unobservable in the figure, we only plot the solid lines here with a zoom-in view for the $a = \mu_1^{(0)}$ case in the inset, showing the difference between them. This also suggests a negligible coupling to

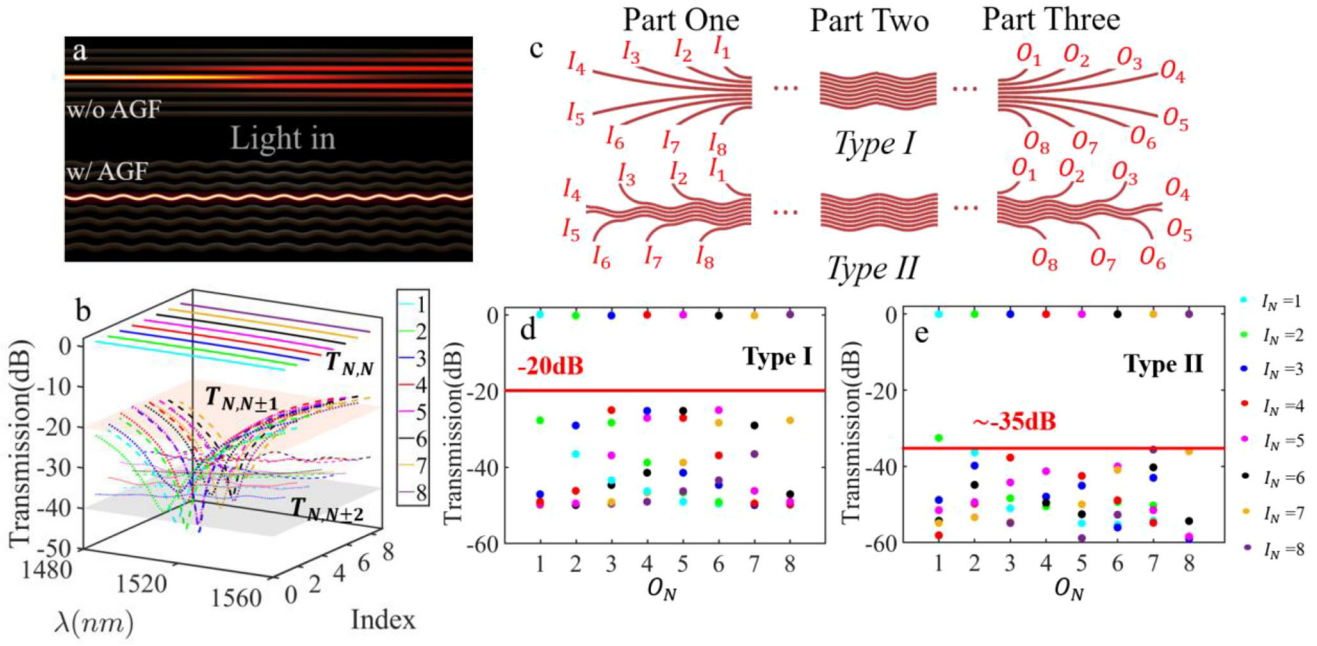

Figure 3. a) The simulated normalized field evolution of the 750 nm-pitched waveguide array with/without the AGF. b) The simulated transmission of the through ($T_{N,N}$), the nearest neighbors ($T_{N,N\pm1}$), and the second nearest neighbors ($T_{N,N\pm2}$) of the proposed 750 nm-pitched waveguide array. Here, the $T_{N,N}$ represents the transmission when light is injected into I_N and detected from O_N. c) Two types of interfaces between the separated waveguides and the dense waveguide array. The simulated transmission of the proposed waveguide array using d) Type I and e) Type II interfaces at the CDT.

surrounding waveguides other than the nearest neighbors, that is, $\kappa_m \ll \kappa_1$ $(m > 1)$. When $a = \mu_1^{(0)}$ (the red dashed line in Figure 2a and the red curve in Figure 2c), $\kappa_{1eq} = 0$ and the dispersion curve becomes flat and nearly a horizontal line, indicating almost no spatial dispersion behavior. We also observe from the inset of Figure 2b that when only considering the coupling from the nearest neighbors κ_1, that is, $\kappa_m = 0$ $(m > 1)$, the energy spectrum of $a = \mu_1^{(0)}$ is exactly a horizontal line, while it is no longer a horizontal line when considering all the coupling, that is, $\kappa_m \neq 0 (m > 1)$ (the dotted line in the inset of Figure 2b). Although the deviation between the two curves is small, it indicates a complete coupling elimination from the nearest neighbors but there still exists a certain amount of coupling from other neighbors. However, such coupling is small as indicated by the very flat curve in Figure 2a,b. In the meantime, the amplitude, which represents the coupling coefficient κ_{1eq}, is positive for $a = 0$, while it's negative for $a = 4$.

Figure 2c explores κ_{1eq} and L_{ceq} as a function of a, where $L_{ceq} = \frac{\pi}{2|\kappa_{1eq}|}$ is the equivalent coupling length when ignoring $\kappa_m (m > 1)$. We observe that $\kappa_{1eq} > 0$ when $a < \mu_1^{(0)}$ while $\kappa_{1eq} < 0$ when $a > \mu_1^{(0)}$, consistent with our discussion above. Note that when $a \to \mu_1^{(0)}$, $\kappa_{1eq} = 0$ and $L_{ceq} \to +\infty$ (the red dashed line), implying a complete cancellation of the coupling from the nearest neighbors. We thus only need to consider $\kappa_m (m > 1)$, which is usually far less than κ_1, for designing a dense waveguide array with low crosstalk.

We design an AGF dense waveguide array on a standard silicon-on-insulator platform with a 220 nm thick silicon nanomembrane. For an AGF with sinusoidal trajectory modulation, the device operates on the CDT point when $J_0(a) = 0$ holds. Therefore, we could take the first zero of the 0th Bessel function $\mu_1^{(0)} \approx 2.405$ and obtain the amplitude $A = \frac{\mu_1^{(0)}}{k_0 n_s \Omega d} \approx \frac{2.405}{k_0 n_s \Omega d}$. We then set the waveguide width at 500 nm and the gap between two adjacent waveguides to 250 nm, corresponding to $d = 750$ nm and $d \leq \frac{\lambda}{2}$ for $\lambda \geq 1.5$ μm. Regarding the trajectory period P, to satisfy the premise that $P\kappa_1 \ll 1$ (see Note S1, Supporting Information, for details), P should be as small as possible. On the other hand, the curvature of the trajectory is $K = \frac{A\Omega^2|\cos(\Omega z)|}{[1+A^2\Omega^2\sin^2(\Omega z)]^{3/2}}$, which has the minimum radius of curvature at the vertices $R_{min} = \frac{1}{A\Omega^2} = \frac{P^2}{4\pi^2 A}$. At the CDT point, A is proportional to P, revealing that R_{min} is proportional to P. Therefore, considering a moderate $R_{min} \approx 5$ μm to provide a negligible bending loss and meet the requirement of $P\kappa_1 \ll 1$, we finally pick up the parameters $R_{min} \approx 5.28$ μm, $P = 10$ μm, and $A = 480$ nm (see Note S2, Supporting Information, for details). The normalized field evolution of the 750 nm-pitched sinusoidal waveguide array is plotted in the lower panel of **Figure 3**a. Compared with the 750 nm-pitched waveguide array without the AGF (upper panel of Figure 3a), the light injected into the middle waveguide travels along the same one with almost no coupling to other waveguides, proving the feasibility of our approach. The simulated results of the 775 nm-pitched and 800 nm-pitched waveguide arrays with/without the AGF are in Note S3, Supporting Information, showing decreasing crosstalk as the waveguide array becomes sparse. The simulated transmission of the proposed dense waveguide array is depicted in Figure 3b. The label "Index" represents the input waveguide index and the $T_{N,N}$ represents the transmission when light is injected into the input waveguide index (I_N) and detected from the output waveguide index (O_N). The crosstalk near the

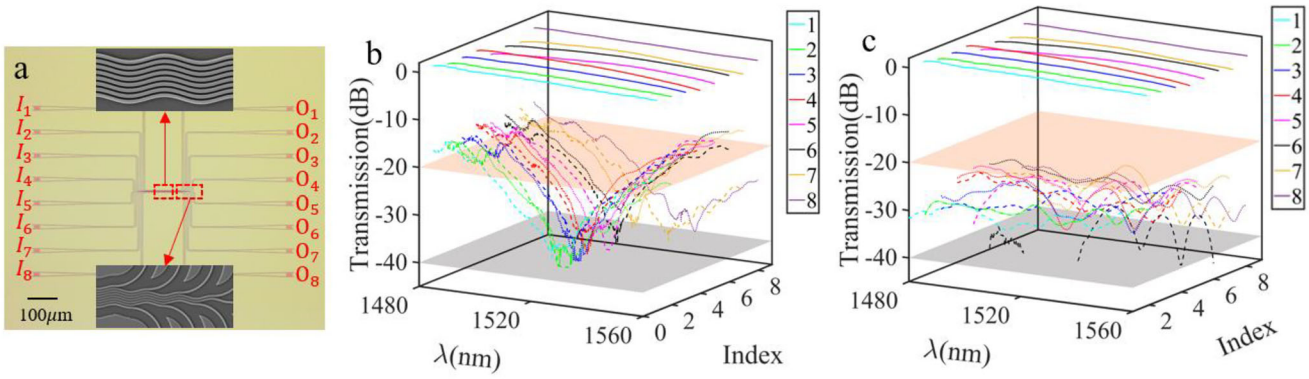

Figure 4. a) The microscope and SEM images of the straight sinusoidal waveguide array. Measured normalized transmission spectra ($T_{N,N}$) of the straight sinusoidal waveguide array (d = 750 nm) and crosstalk from b) the nearest neighbors ($T_{N,N\pm1}$) and c) the second nearest neighbors ($T_{N,N\pm2}$). The orange and gray planes correspond to −20 and −40 dB, respectively.

CDT is below −35 dB, and the bandwidth of −20 dB crosstalk is about 70 nm. Slightly higher crosstalk at longer wavelengths is observed because of less confinement at the longer wavelengths. Note that, due to the wavelength-dependent variable a, there is a valley at each transmission spectrum from the nearest neighbors ($T_{N,N\pm1}$), corresponding to the CDT point, which is the feature of the sinusoidal array. The transmission from the second nearest neighbors ($T_{N,N\pm2}$) is about −37 dB near the CDT and grows up gradually from −38 to −25 dB as the wavelength increases.

The interface (Part One and Part Three in Figure 3c) between the separated waveguides and the proposed dense waveguide array (Part Two) is crucial as a smooth transition would avoid extra crosstalk. Figure 3c shows two types of interfaces. For Type I (the upper panel of Figure 3c), the separated waveguides transition to the dense waveguide array with different bending radii directly, and the corresponding transmission at CDT is plotted in Figure 3d, showing crosstalk below −20 dB for all the eight channels. However, such an interface may result in additional crosstalk for a large-scale waveguide array due to the reduction of bending radius mismatch ratio and consequent the diminishment of propagation constant mismatch between adjacent waveguides and longer propagating length, especially for the ports in the middle. To solve this issue, we design the Type II interface (the lower panel of Figure 3c) by accessing the array at the vertices with a fixed bending radius of 5 μm. This structure could avoid coupling from nearby waveguides even for a large-scale array. The transmission in Figure 3e shows a below −35 dB crosstalk for all the channels, a 15 dB improvement compared with Type I. Moreover, the scalability of Type II guarantees a low extra crosstalk transition for a large-scale dense waveguide array.

We fabricate (see ref. [35] for details) and characterize the straight sinusoidal waveguide arrays with different pitches, that is, d = 750, 775, and 800 nm. **Figure 4**a shows the microscope image of the fabricated device with the zoom-in images of the straight sinusoidal waveguide array and the interface in the upper and lower insets, respectively. After coupling into the chip (see Note S6, Supporting Information, for details), light runs along the single-mode strip waveguide and enters the dense waveguide array (the upper inset of Figure 4a), which is 100 μm long in horizontal, through the specially designed interface (the lower inset of Figure 4a). The output transmission from the nearest ($T_{N,N\pm1}$) and the second nearest ($T_{N,N\pm2}$) waveguides represents the crosstalk of the nearest and the second nearest neighbors. A 100 μm long single-mode strip waveguide connected directly to the input and output grating couplers is fabricated on the same chip as a reference. Figure 4b shows the normalized transmission ($T_{N,N}$) of the sinusoidal waveguide array with a pitch of d = 750 nm and the crosstalk of the nearest neighbors. A significant crosstalk suppression is observed at the wavelength of ≈1520 nm with crosstalk lower than −35 dB, corresponding to the aforementioned CDT point. The AGF-induced crosstalk suppression happens in the entire wavelength range from 1480 to 1560 nm with a 40 nm bandwidth of crosstalk below −20 dB. Figure 4c provides the normalized transmission of the same waveguide array and the crosstalk of the second nearest neighbors. Compared with the nearest neighbors, the spectra are much flatter with an 80 nm bandwidth of crosstalk below −20 dB, and the crosstalk near the CDT point is about −30 dB. Therefore, it is fair to conclude that the maximum crosstalk suppression is limited by the second nearest neighbors while the bandwidth limitation is from the nearest neighbors. The normalized transmission spectra ($T_{N,N}$) are close to 0 dB, indicating a negligible insertion loss. The measured transmission spectra of the 775 nm-pitched and 800 nm-pitched waveguide arrays with the AGF are shown in Note S3, Supporting Information.

3. The Bent Sinusoidal Waveguide Array

Bending a dense waveguide array is not trivial, especially for on-chip delay lines. It is well known that bending could introduce bending-radius-dependent propagation constant variations. This effect has been exploited to design a dense waveguide array.[19] However, due to the inverse ratio between $\Delta\beta$ and the bending radius, such a waveguide array has a scaling issue. To address it, we apply the sinusoidal AGF to a bent waveguide array. The structure of the proposed bent waveguide array is depicted in **Figure 5**a, where the bent waveguide array with the AGF (left) has the same cross section as the straight sinusoidal waveguide array discussed in previous sections. For comparison, we plot the bent waveguide array without an AGF on the right side. As displayed in Figure 5a, similar to the straight sinusoidal waveguide array, the AGF also induces additional phases in the bent waveg-

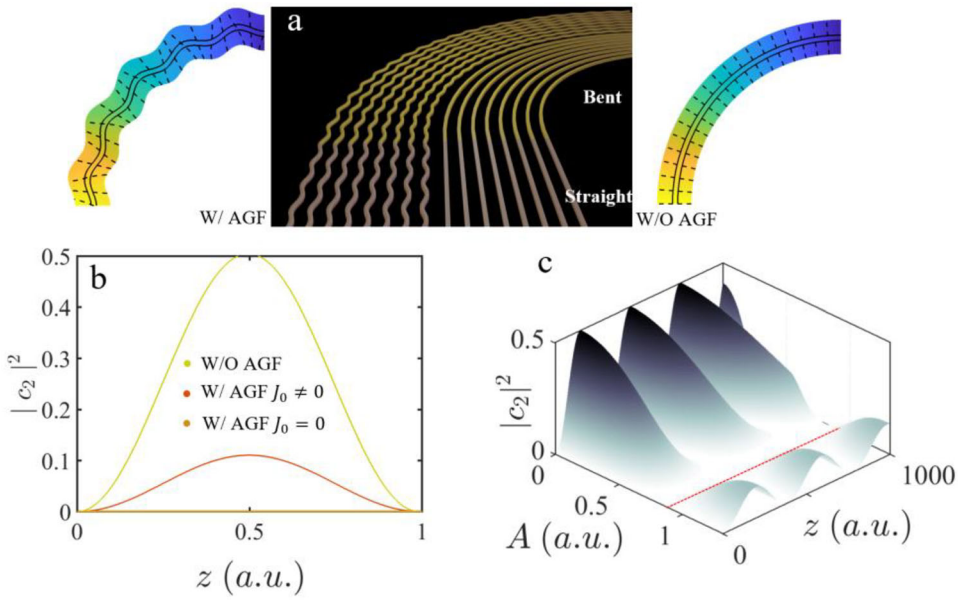

Figure 5. a) Schematic of the bent waveguide arrays with (left)/without (right) the AGF and their corresponding phase distribution of the eigenstate, where the dashed lines correspond to the equiphase surfaces. b) Normalized coupled power $|c_2|^2$ as a function of the normalized propagation length z, where the yellow, red, and brown curves correspond to the system without an AGF, with an AGF and $J_0(k_0 n_s \Omega A d) \neq 0$, and with an AGF and $J_0(k_0 n_s \Omega A d) = 0$, respectively. Note that z is the scaled one coupling cycle length. c) Normalized coupled power $|c_2|^2$ as a function of the normalized propagation length z and modulation amplitude A, where the red dotted line corresponds to $J_0(k_0 n_s \Omega A d) = 0$ (the CDT point).

uide array. The equiphase surfaces become curved and tilted in the AGF arrays (the left panel of Figure 5a), other than a series of planes perpendicular to the propagation direction in the waveguide array without an AGF (the right panel of Figure 5a). These tilted equiphase surfaces would affect the coupling coefficients, resulting in AGF-induced quantum tunneling suppression.

Assuming the ith waveguide trajectory in the polar coordinate as $r_i(\theta)$, we transform the bent waveguide array from uyv space into a straight waveguide array in xyz space using conformal transformation (from uyv space to xyz space)[36] first and then analyze it by a gauge transformation (from xyz space to $x'yz$ space). Since all the waveguides in the array are different after the conformal transformation, the Bloch theory is not applicable. We then start from a two-waveguide system, and the conclusion can be extended to a waveguide array. For a two-waveguide system with the same AGF in the xyz space, $x_0(z)$, the coupled wave equation in the xyz space is (see Note S4, Supporting Information, for details):

$$i\frac{\partial}{\partial z}\begin{bmatrix} c_1 \\ c_2 \end{bmatrix} = \begin{bmatrix} \rho_1 + \delta & \kappa_{1av\delta} \\ \kappa_{2av\delta} & \rho_2 - \delta \end{bmatrix}\begin{bmatrix} c_1 \\ c_2 \end{bmatrix} \tag{2}$$

where $\rho_{1,2}$ are the self-coupling coefficients. $\kappa_{1av\delta} = \overline{\kappa_1(z)exp(-2\delta z)} = \frac{\Omega}{2\pi}\int_0^{\frac{2\pi}{\Omega}} \kappa_1(z)exp(-2\delta z)dz$ and $\kappa_{2av\delta} = \overline{\kappa_2(z)exp(-2\delta z)} = \frac{\Omega}{2\pi}\int_0^{\frac{2\pi}{\Omega}} \kappa_2(z)exp(-2\delta z)dz$ are the equivalent mutual coupling coefficient of the bent waveguide array, of which $\kappa_{1,2}\ (z) = exp[i\beta_{2,1}z - i\beta_{1,2}z \mp ik_0 n_s \dot{x}_1(z)d]$ is the mutual coupling coefficient. $c_1 = a_1(z)\exp(-i\delta z)$ and $c_2 = a_2(z)\exp(i\delta z)$, where $a_1(z)$ and $a_2(z)$ are the complex amplitude of the quantum states in the two-waveguide system. $\delta = \frac{\beta_2 - \beta_1}{2}$ represents the mismatch between the two states, and $\beta_{1,2}$ are the corresponding propagation constants in the xyz space.

When the AGF for the two waveguides is identical in the xyz space, that is, $A_1 = A_2 = A$, we have $\kappa_{1,2av\delta} = \kappa_{1,2}J_0(k_0 n_s \Omega A d)$. The expression of $\kappa_{1,2av\delta}$ implies that in the bent waveguide array with the sinusoidal AGF, we have not only a propagation constant mismatch δ but also a lower coupling coefficient $\kappa_{1,2av\delta}$ by a factor of $J_0(k_0 n_s \Omega A d)$. These two factors contribute to the coupling reduction, that is, crosstalk suppression.

To understand the propagation characteristics more intuitively, we plot the normalized coupled power $|c_2|^2$ as a function of the normalized propagation length z in Figure 5b under the initial condition of $c_1(0) = 1$ and $c_2(0) = 0$ ($|c_1|^2 = 1 - |c_2|^2$). For visualization, we only draw one coupling cycle for the three cases in Figure 5b (see Note S4, Supporting Information, for details). The yellow, red, and brown curves correspond to the system without an AGF, with an AGF and $J_0(k_0 n_s \Omega A d) \neq 0$, and with an AGF and $J_0(k_0 n_s \Omega A d) = 0$, respectively.

For the conventional bent waveguides without an AGF, that is, $A = 0$ (the right panel of Figure 5a), bending induces a bending-radius-dependent propagation constant variation, that is, $\beta_{1,2} = \beta\frac{R_{1,2}}{R_0}$ ($\beta_{1,2}$ is the propagation constant in xyz space), that generates propagation constant mismatches, that is, $\beta_1 \neq \beta_2$, and quenches the couplings. However, such an effect gradually fades for a large-scale bent waveguide array as the increasing R shrinks the propagation constant mismatches. Applying a sinusoidal AGF ($A \neq 0$, the left panel of Figure 5a) to the two-waveguide system triggers a coupling depression by a scale factor of $J_0(k_0 n_s \Omega A d)$, as depicted by the much lower amplitude of the red curve in Figure 5b. Further adjusting the A to fulfill $J_0(k_0 n_s \Omega A d) = 0$ will lead to an almost complete coupling suppression, as depicted by the

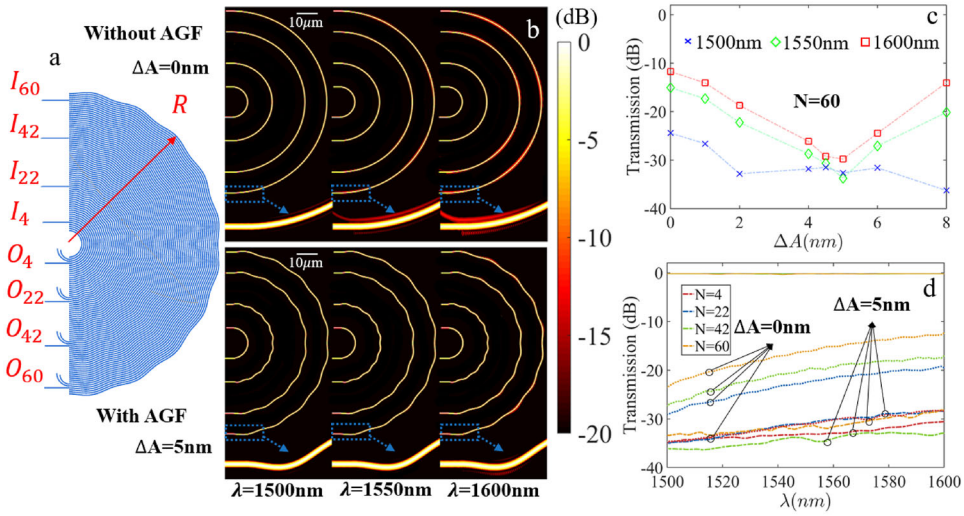

Figure 6. a) Schematic of the bent sinusoidal waveguide array. b) Normalized field evolutions of the bent waveguide arrays with (upper panel) and without (lower panel) the AGF. Three columns correspond to the wavelength of 1500, 1550, and 1600 nm, respectively. The insets show the zoom-in views of the electrical fields in the outer waveguides. c) Simulated crosstalk for the AGF with different ΔA when light is injected into the 60th waveguide. d) Simulated transmission spectra of bent dense waveguide arrays with AGF ($\Delta A = 5$ nm) and without the AGF. The solid, dotted, and dash-dotted curves correspond to the transmission of the through ports, and the crosstalk of waveguide arrays with and without the AGF, respectively.

brown curve in Figure 5b, which nearly coincides with the x-axis. The coupling, that is, the crosstalk, is reduced by several orders of magnitude compared to the $J_0(k_0 n_s \Omega A d) \neq 0$ case, indicating a feasible approach to design a bent waveguide array with extremely low crosstalk.

Combining all cases discussed above, we plot $|c_2|^2$ as a function of A and z in Figure 5c. Because of the propagation constant mismatch caused by different bending radii, $|c_2|^2_{\max}$ is always less than 1. In the meantime, $|c_2|^2_{\max}$ varies with A, owing to the AGF-affected coupling coefficient variations. When $A = 0$, the $|c_2|^2_{\max}$ is the largest, proving the AGF-induced coupling coefficient reduction. Especially when $J_0(k_0 n_s \Omega A d) = 0$ (the red dotted line), $|c_2|^2_{\max}$ is very close to 0 (see Note S4, Supporting Information, for details), providing an operating point for us to design a high-density waveguide array with low crosstalk.

Moreover, based on the coupling wave theory above, we can calculate the bandwidth of the straight/bent two-waveguide system. And the results indicate that a bent waveguide system has a broader bandwidth than the straight one (see Note S5, Supporting Information, for details). **Figure 6**a illustrates the proposed bent sinusoidal waveguide array, including two 90° bends. The array consists of 64 sinusoidal waveguides with a waveguide width of 500 nm and minimum bending radii of 5 μm. The gap between two adjacent waveguides is 250 nm to implement a 750 nm pitch which is less than half of the working wavelengths. To achieve low crosstalk, we design all the waveguides with the same AGF in the xyz space, that is, a fixed $A_i = R_0 \frac{A_{uv,i}}{R_i}$ for all the waveguides. Here, R_0 is a constant, and R_i is the bending radius of the ith waveguide, $A_{uv,i}$ is the curve amplitude in the uyv space. For a 64-channel bent waveguide array with 750 nm pitch, the bending radii range from 5 to 52.25 μm with a step of 750 nm. Moreover, we have $\Delta A = A_{uv,i+1} - A_{uv,i} = 5$ nm, that is, $\frac{A_{uv,i}}{R_i} = \frac{\Delta A}{d} = \frac{1}{150}$. Figure 6b gives the electrical field evolutions for a bent half-wavelength pitched waveguide array with/without an AGF. We pick up four individual waveguides (4th, 22nd, 42nd, and 60th) randomly, representing waveguides with different bending radii, for light injection and collection. For the array without an AGF (the upper panel of Figure 6b), we observe almost isolated guiding at all three wavelengths (1500, 1550, and 1600 nm) for the waveguides with small bending radii, that is, the 4th and 22nd waveguides. However, for the outer waveguides with larger bending radii, that is, the 42nd and 60th waveguides, clear couplings are evidenced in the zoom-in views and the periodical bright–dark distributions. This effect becomes more evident for longer wavelengths due to the longer decay length of the evanescent waves, implying the limitation of such an approach. In comparison, for the array with the AGF (the lower panel of Figure 6b), the coupling is significantly suppressed with negligible crosstalk for all waveguides at the three wavelengths, as shown in the zoom-in views.

Figure 6c shows the crosstalk variations for different ΔA. We choose the 60th waveguide as the representative for waveguides with a larger bending radius and scan ΔA from 0 to 8 nm. When $\Delta A = 0$, all the waveguides have the same sinusoidal amplitude. However, due to the different bending-radius-induced propagation constant variation, this design does not reach our expectation that the crosstalk is still about −15 dB at 1550 nm. As ΔA increases, it gradually compensates for the propagation constant variations-induced decoupling and achieves minimum crosstalk ≈−30 dB at the CDT point when $\Delta A = 5$ nm.

The simulated transmissions of the bent waveguide arrays with ($\Delta A = 5$ nm) and without the AGF are plotted in Figure 6d, where the solid, dash-dotted, and dotted curves correspond to the transmission of the through ports, and the crosstalk of the waveguide array with and without the AGF, respectively. For the array without the AGF, only the 4th port (the red dotted line) has crosstalk less than −25 dB for wavelengths from 1500 to 1600 nm due to larger propagation constant mismatch for small radii. As the radius increases, the mismatch decreases, and the crosstalk

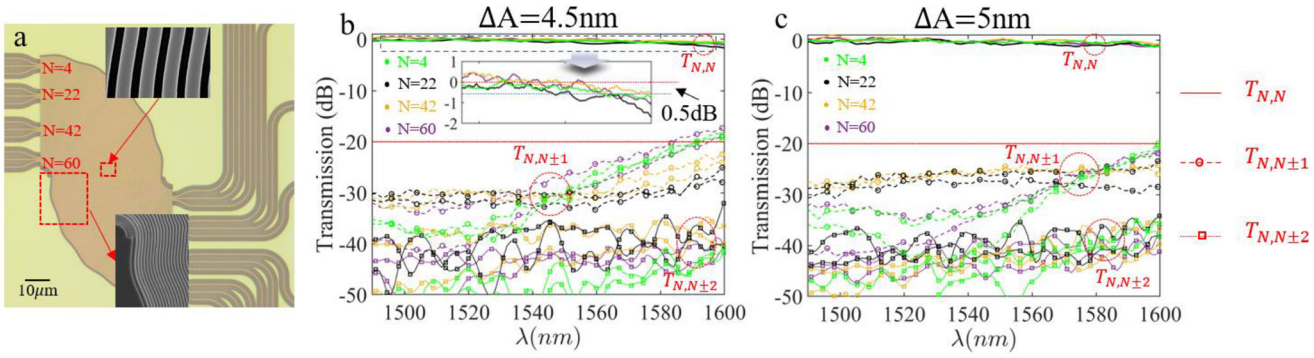

Figure 7. a) The microscope and SEM images of the bent sinusoidal waveguide array. The array consists of two back-to-back connected identical 90° bending arrays. Measured normalized transmission spectra ($T_{N,N}$) and crosstalk ($T_{N,N\pm1}$ and $T_{N,N\pm2}$) of the bent sinusoidal waveguide array (d = 750 nm) with b) ΔA = 4.5 nm and c) ΔA = 5 nm.

increases. For the 60th port (the yellow line), the crosstalk is even higher than −15 dB at longer wavelengths. As a comparison, applying the AGF to a bent dense waveguide array crushes the crosstalk to about −28 dB for wavelengths from 1500 to 1600 nm. This design with such an impressive performance not only solves the bending issue for a dense waveguide array with a large scale but also remarkably enlarges the working bandwidth.

The performance of the bent sinusoidal waveguide arrays is characterized. **Figure 7**a shows the microscope image of the proposed waveguide array with the zoom-in SEM images in the insets. Four ports, that is, the 4th, 22nd, 42nd, and 60th ports are chosen to characterize the crosstalk under different bending radii. This array consists of two back-to-back connected identical 90° bending arrays. We plot the measured crosstalk of two waveguide arrays with ΔA of 4.5 and 5 nm in Figures 7b and 7c respectively. The solid lines represent the normalized output power from the through ports and the dotted lines correspond to the output from the $T_{N,N\pm1}$ and $T_{N,N\pm1}$ in the two waveguide arrays. Both of them exhibit excellent crosstalk suppression and negligible insertion losses. While the one with ΔA = 4.5 nm achieves −30 dB crosstalk suppression from 1480 to 1550 nm, the one with ΔA = 5 nm possesses a larger than 100 nm bandwidth for the crosstalk lower than −25 dB and entire measured wavelength range, from 1480 to 1600 nm, for the crosstalk lower than −20 dB. This demonstration proves the effectiveness of our bent sinusoidal waveguide arrays in crosstalk suppression and bandwidth enlargement. It also provides a solution for flexibly routing a large-scale waveguide array.

4. Summary

We develop an AGF-based coupling mechanism to suppress the crosstalk inside a half-wavelength-pitched waveguide array to −30 dB. The AGF-induced additional phases tilt the equiphase surfaces and complexify the coupling coefficients that modify the band structure and inhibit the quantum tunnel effect. By modulating the trajectory of waveguide arrays, we apply the AGF to the optical domain to suppress the coupling among waveguides. The AGF-induced exceptional coupling is observed with minimum crosstalk of ←35 dB at the wavelength of 1520 nm in the 750 nm pitched straight waveguide array with negligible insertion loss, of which the pitch is even smaller than half of the wavelength. Further optimizing the design, we also demonstrate 90° bent half-wavelength-pitched waveguide arrays, consisting of 64 waveguides and possessing −30 dB crosstalk suppression from 1480 to 1550 nm and >100 nm bandwidth for the crosstalk lower than −25 dB, respectively. Such bent waveguide arrays enable both broadband crosstalk suppression and on-chip flexible routing. Our devices enable significant integration density improvement of the on-chip photonic circuits and open up opportunities for advancing device performance, such as half-wavelength-pitched OPA, high-density on-chip optical interconnecting, and ultra-dense space-division multiplexing.

Supporting Information

Supporting Information is available from the Wiley Online Library or from the author.

Acknowledgements

P.Z. and Ti.L. contributed equally to this work. The research was sponsored by the Natural Science Foundation of Shanghai (21ZR1443100), the National Natural Science Foundation of China (NSFC) (61705099), and the Science and Technology Commission of Shanghai Municipality (Y7360k1D01). The authors thank the ShanghaiTech University Quantum Device Lab (SQDL) for technique support.

Conflict of Interest

The authors declare no conflict of interest.

Data Availability Statement

The data that support the findings of this study are available from the corresponding author upon reasonable request.

Keywords

artificial gauge fields, integrated photonics, silicon photonics, waveguide arrays

Received: December 6, 2022
Revised: April 2, 2023
Published online:

[1] H. Lee, T. Chen, J. Li, O. Painter, K. J. Vahala, *Nat. Commun.* **2012**, *3*, 867.
[2] X. Ji, X. Yao, Y. Gan, A. Mohanty, M. A. Tadayon, C. P. Hendon, M. Lipson, *APL Photonics* **2019**, *4*, 090803.
[3] M. R. Kossey, C. Rizk, A. C. Foster, *APL Photonics* **2018**, *3*, 011301.
[4] C. T. Phare, M. C. Shin, J. Sharma, S. Ahasan, H. Krishnaswamy, M. Lipson, in *Conf. on Lasers and Electro-Optics, OSA Technical Digest (online)*, Optical Society of America, Washington, DC **2018**, p. SM3I2.
[5] L.-M. Leng, Y. Shao, P.-Y. Zhao, G.-F. Tao, S.-N. Zhu, W. Jiang, *Phys. Rev. Appl.* **2021**, *15*, 014019.
[6] W. Xu, L. Zhou, L. Lu, J. Chen, *Opt. Express* **2019**, *27*, 3354.
[7] D. J. Richardson, J. M. Fini, L. E. Nelson, *Nat. Photonics* **2013**, *7*, 354.
[8] D. A. B. Miller, *Proc. IEEE* **2009**, *97*, c1166.
[9] R. G. Beausoleil, J. H. Ahn, N. L. Binkert, A. Davis, Q. Xu, in *IEEE Symp. on High Performance Interconnects*, IEEE, Piscataway, NJ **2008**.
[10] W. Bogaerts, S. K. Selvaraja, P. Dumon, J. Brouckaert, K. D. Vos, D. V. Thourhout, R. Baets, *IEEE J. Sel. Top. Quantum Electron.* **2010**, *16*, 33.
[11] K. Okamoto, *IEEE J. Sel. Top. Quantum Electron.* **2014**, *20*, 248.
[12] V. J. Sorger, Z. Ye, R. F. Oulton, Y. Wang, G. Bartal, X. Yin, X. Zhang, *Nat. Commun.* **2011**, *2*, 331.
[13] J. B. Khurgin, *Nat. Nanotechnol.* **2015**, *10*, 2.
[14] J. B. Khurgin, *Philos. Trans. R. Soc., A.* **2017**, *375*, 20160068.
[15] B. Shen, R. Polson, R. Menon, *Nat. Commun.* **2016**, *7*, 13126.
[16] S. Jahani, S. Kim, J. Atkinson, J. C. Wirth, F. Kalhor, A. A. Noman, W. D. Newman, P. Shekhar, K. Han, V. Van, R. G. DeCorby, L. Chrostowski, M. Qi, Z. Jacob, *Nat. Commun.* **2018**, *9*, 1893.
[17] L. Wang, Z. Chen, H. Wang, A. Liu, P. Wang, T. Lin, X. Liu, H. Lv, *Opt. Lett.* **2019**, *44*, 3266.
[18] W. Song, R. Gatdula, S. Abbaslou, M. Lu, A. Stein, W. Y. Lai, J. Provine, R. F. Pease, D. N. Christodoulides, W. Jiang, *Nat. Commun.* **2015**, *6*, 7027.
[19] H. Xu, Y. Shi, *Opt. Lett.* **2016**, *41*, 4815.
[20] S. Longhi, M. Marangoni, M. Lobino, R. Ramponi, P. Laporta, E. Cianci, V. Foglietti, *Phys. Rev. Lett.* **2006**, *96*, 243901.
[21] A. Szameit, I. L. Garanovich, M. Heinrich, A. A. Sukhorukov, F. Dreisow, T. Pertsch, S. Nolte, A. T¨unnermann, Y. S. Kivshar, *Nat. Phys.* **2009**, *5*, 271.
[22] A. Szameit, I. L. Garanovich, M. Heinrich, A. A. Sukhorukov, F. Dreisow, T. Pertsch, S. Nolte, A. Tunnermann, S. Longhi, Y. S. Kivshar, *Phys. Rev. Lett.* **2010**, *104*, 223903.
[23] D. H. Dunlap, V. M. Kenkre, *Phys. Rev. B* **1986**, *34*, 3625.
[24] I. L. Garanovich, A. Szameit, A. A. Sukhorukov, T. Pertsch, W. Krolikowski, S. Nolte, D. Neshev, A. Tuennermann, Y. S. Kivshar, *Opt. Express* **2007**, *15*, 9737.
[25] M. C. Rechtsman, J. M. Zeuner, Y. Plotnik, Y. Lumer, D. Podolsky, F. Dreisow, S. Nolte, M. Segev, A. Szameit, *Nature* **2013**, *496*, 196.
[26] E. Lustig, S. Weimann, Y. Plotnik, Y. Lumer, M. A. Bandres, A. Szameit, M. Segev, *Nature* **2019**, *567*, 356.
[27] X. Cheng, C. Jouvaud, X. Ni, S. H. Mousavi, A. Z. Genack, A. B. Khanikaev, *Nat. Mater.* **2016**, *15*, 542.
[28] L. D. Tzuang, K. Fang, P. Nussenzveig, S. Fan, M. Lipson, *Nat. Photonics* **2014**, *8*, 701.
[29] Q. Lin, S. H. Fan, *Phys. Rev. X* **2014**, *4*, 031031.
[30] Y. Lumer, M. A. Bandres, M. Heinrich, L. J. Maczewsky, H. HerzigSheinfux, A. Szameit, M. Segev, *Nat. Photonics* **2019**, *13*, 339.
[31] X. Yi, H. Zeng, S. Gao, C. Qiu, *Opt. Express* **2020**, *28*, 37505.
[32] W. Song, T. Li, S. Wu, Z. Wang, C. Chen, Y. Chen, C. Huang, K. Qiu, S. Zhu, Y. Zou, T. Li, *Phys. Rev. Lett.* **2022**, *129*, 053901.
[33] F. Grossmann, T. Dittrich, P. Jung, P. Hanggi, *Phys. Rev. Lett.* **1991**, *67*, 516.
[34] W. Song, H. Li, S. Gao, C. Chen, S. Zhu, T. Li, *Adv. Photonics* **2020**, *2*, 036001.
[35] A. Zhang, L. Xia, T. Li, C. Chang, P. Zhou, X. Xu, Y. Zou, *Opt. Lett.* **2021**, *46*, 5000.
[36] M. Heiblum, J. Harris, *IEEE J. Quantum Electron.* **1975**, *11*, 75.